Electromagnetic induction by a finite electric dipole source over a 2-D earth

Martyn J. Unsworth*, Bryan J. Travis‡, and Alan D. Chave**

ABSTRACT

A numerical solution for the frequency domain electromagnetic response of a two-dimensional (2-D) conductivity structure to excitation by a three-dimensional (3-D) current source has been developed. The fields are Fourier transformed in the invariant conductivity direction and then expressed in a variational form. At each of a set of discrete spatial wavenumbers a finite-element method is used to obtain a solution for the secondary electromagnetic fields. The finite element uses exponential elements to efficiently model the fields in the far-field. In combination with an iterative solution for the along-strike electromagnetic fields, this produces a considerable reduction in computation costs. The numerical solutions for a horizontal electric dipole are computed and shown to agree with closed form expressions and to converge with respect to the parameterization. Finally some simple examples of the electromagnetic fields produced by horizontal electric dipole sources at both the seafloor and air-earth interface are presented to illustrate the usefulness of the code.

INTRODUCTION

Major advances have been made in the numerical modeling of electromagnetic induction in the earth in recent years due to the ever increasing power of digital computers and numerical algorithms. However, a problem that has received very little attention in the geophysical literature is the general, three-dimensional (3-D) or finite source over an earth whose conductivity varies in only two dimensions, the so-called 2.5-D problem. The 2.5-D problem represents an important geophysical situation since many geological targets may be approximately 2-D, but practical electromagnetic sources are of necessity 3-D. In such cases, a fully 3-D medium is not needed and the computational costs can be greatly reduced by solving just the 2.5-D problem.

A limited number of solutions have appeared in the literature which are relevant to 2.5-D electrical and electromagnetic problems. The DC resistivity and induced polarization problems were addressed in Coggon (1971), Snyder (1976), and Fox et al. (1980). The first published theoretical finite-element (FE) derivation for the 2.5-D electromagnetic problem was in Coggon (1971). Stoyer and Greenfield (1976) used a finite-difference method to compute the frequency-domain response of a 2-D earth to a vertical magnetic dipole source. This approach was successfully applied by Stoyer (1975) to groundwater exploration problems. Lee (1978) and Lee and Morrison (1985) presented a finite-element solution for the fields induced by a magnetic dipole over a 2-D earth and found good agreement with analog results, but the method was computationally intensive. The 2.5-D time-domain problem has been addressed by Everett (1990) who describes a solution for a transient seafloor exploration system and by Moghaddam et al. (1991) who present a solution for ground-penetrating radar.

Recent developments in finite-element methodology should be able to produce an algorithm that can accurately and efficiently model the electromagnetic response of complex 2-D conductivity structures to 3-D sources. In this paper, the 2.5-D differential equations will be defined and then the corresponding variational forms will be used to generate the finite-element equations. The finite-element methodology will be described in detail, as will the tests used to validate the code and its numerical stability. The paper concludes with some simple seafloor examples.

THEORY

Governing Equations

The total electric and magnetic fields (E and B) generated by a specified source current distribution $\mathbf{J}_s$ satisfy the pre-Maxwell equations in which the magnetic effect of displacement current is neglected

$$\nabla \cdot \mathbf{B} = 0 \tag{1}$$

$$\nabla \wedge \mathbf{E} = -\frac{\partial \mathbf{B}}{\partial t}, \tag{2}$$

and

$$\nabla \wedge \mathbf{B} - \mu_0 \sigma \mathbf{E} = \mu_0 \mathbf{J}_s, \tag{3}$$

where σ is the electrical conductivity which is assumed to vary in two dimensions and μ_0 is the magnetic permeability of free space. For a point electromagnetic source, $\mathbf{J}_s$ is singular and difficult to represent accurately by a discrete formulation. This problem is easily overcome by separating the total electric and magnetic fields into their primary and secondary components. The primary fields can be calculated for a simple, one-dimensional (1-D) conductivity structure, $\sigma_0(z)$. Thus, equations (2) and (3) also govern primary fields, when $\sigma = \sigma(z)$ and when subtraction equations obtained for the secondary fields are:

$$\nabla \wedge \mathbf{E}^s = -\frac{\partial \mathbf{B}^s}{\partial t} \tag{4}$$

$$\nabla \wedge \mathbf{B}^s - \mu_0 \sigma \mathbf{E}^s = \mu_0 \Delta\sigma \mathbf{E}^p, \tag{5}$$

where $\Delta\sigma = \sigma - \sigma_0$ is the difference between the total 2-D conductivity and the 1-D background conductivity used to calculate the primary fields. Providing that $\Delta\sigma = 0$ at the source, the singular source term has been replaced by the nonsingular function $\Delta\sigma \mathbf{E}^p$ which is distributed throughout the solution space. Note that ha is not constrained to be either small or positive.

A Cartesian coordinate system is defined with $\hat{z}$ vertically upwards and the conductivity invariant in the $\hat{x}$-direction. Since the conductivity varies in only two dimensions, the solution can be simplified further by Fourier transforming each field component in the i-direction, with the Fourier transform of each component defined as

$$\hat{F}(k_x, y, z) = \int_{-\infty}^{\infty} dx \, e^{ik_x x} F(x, y, z). \tag{6}$$

Throughout this paper a hat (^) will be used to denote quantities in the Fourier transform domain. With a harmonic time variation proportional to $e^{-i\omega t}$ for each field component, equations (4) and (5) can be written in Cartesian form as

$$-ik_x \hat{E}_y^s - \partial_y \hat{E}_x^s - i\omega \hat{B}_z^s = 0, \tag{7}$$

$$\partial_y \hat{B}_z^s - \partial_z \hat{B}_y^s - \mu_0 \sigma \hat{E}_x^s = \mu_0 \Delta\sigma \hat{E}_x^p, \tag{8}$$

$$\partial_z \hat{E}_x^s + ik_x \hat{E}_z^s - i\omega \hat{B}_y^s = 0, \tag{9}$$

$$-ik_x \hat{B}_y^s - \partial_y \hat{B}_x^s - \mu_0 \sigma \hat{E}_z^s = \mu_0 \Delta\sigma \hat{E}_z^p, \tag{10}$$

$$\partial_y \hat{E}_z^s - \partial_z \hat{E}_y^s - i\omega \hat{B}_x^s = 0, \tag{11}$$

$$\partial_z \hat{B}_x^s + ik_x \hat{B}_z^s - \mu_0 \sigma \hat{E}_y^s = \mu_0 \Delta\sigma \hat{E}_y^p, \tag{12}$$

where k_x is the along-strike wavenumber. If the source is invariant in the t-direction ($k_x = 0$), then it is well known that two independent electromagnetic modes can be treated separately, as in magnetotellurics or for an infinitely long wire source. In this limit the transverse electric (TE) or $E_\parallel$ mode is defined by equations (7) to (9) and only has an electric field component in the invariant direction ($\hat{x}$) of conductivity. The transverse magnetic (TM) or $E_\parallel$ mode is defined by equations (10) to (12) and has a magnetic component only in the invariant conductivity direction ($\hat{x}$) while the electric field is confined to the (y , z) plane. The solution of these zero-wavenumber problems gives useful insights into the physics of electromagnetic induction, but the results must be applied cautiously to the interpretation of data from 3-D sources, since the reduction in dimension fails to represent the complete inductive process.

To compute the response for a finite source, a range of nonzero k_x values must be considered to represent the fields in the Fourier domain. When k_x is nonzero, independent $E_\parallel$ and $E_\perp$ modes no longer exist; they are effectively coupled by the source so that the fields vary in three dimensions. Equations (7) to (12) may be rearranged to yield coupled equations for $\hat{E}_x^s$ and $\hat{B}_x^s$, the secondary, along-strike fields in the Fourier transform domain.

$$\nabla \cdot \left(\frac{\mu_0 \sigma \nabla \hat{E}_x^s}{\gamma^2}\right) - \mu_0 \sigma \hat{E}_x^s = \mu_0 \Delta\sigma \hat{E}_x^p - ik_x \nabla \cdot \left(\frac{\Delta\sigma \hat{\mathbf{E}}^p}{\gamma^2}\right)$$
$$+ ik_x \left[\nabla \hat{B}_x^s \wedge \nabla\left(\frac{1}{\gamma^2}\right)\right] \cdot \hat{\mathbf{x}} \tag{13}$$

$$\nabla \cdot \left(\frac{i\omega \nabla \hat{B}_x^s}{\gamma^2}\right) - i\omega \hat{B}_x^s = i\omega\mu_0 \nabla \wedge \left(\frac{\Delta\sigma \hat{\mathbf{E}}^p}{\gamma^2}\right) \cdot \hat{\mathbf{x}}$$
$$+ ik_x \left[\nabla \hat{E}_x^s \wedge \nabla\left(\frac{1}{\gamma^2}\right)\right] \cdot \hat{\mathbf{x}}, \tag{14}$$

where $\gamma^2 = k_x^2 - i\omega\mu_0\sigma$, $\hat{\mathbf{x}}$ is a unit vector in the x-direction and $\nabla = (0, \partial_y, \partial_z)$. The coupling term is proportional to k_x so that at zero-wavenumber the modes are independent. With a nonzero wavenumber, a minimum of two field components must be calculated at a point to represent the 3-D electromagnetic fields, whereas only one suffices for the zero-wavenumber case.

Finite-element formulation

The 2.5-D induction problem can also be written in a variational form that allows the finite-element equations to be derived. Suppose that a field $V(y, z)$ satisfies the differential equation $\mathcal{D}V = f$ in a region Ω with boundary conditions $V = f_0$ on the perimeter $\partial\Omega$ where $\mathcal{D}$ is a differential operator, f is a specified source function, and fo is a known function. The calculus of variations, e.g., Clegg (1968), shows that solving the differential equation is equivalent to finding a function V that minimizes the Lagrangian

$$\mathscr{L} = \int^{\Omega} L(V, \partial_y V, \partial_z V) \, dy \, dz, \qquad (15)$$

where L, the Lagrange density, satisfies the Euler-Lagrange equation,

$$\partial_y \left[\frac{\partial L}{\partial(\partial_y V)} \right] + \partial_z \left[\frac{\partial L}{\partial(\partial_z V)} \right] = \frac{\partial L}{\partial V}. \qquad (16)$$

Equations (13) and (14) are of the form

$$-\nabla \cdot (a(y, z)\nabla V) + b(y, z)V = f(y, z) \qquad (17)$$

which can easily be shown to have Lagrange densities of the form

$$L = \frac{a}{2} (\partial_y V)^2 + \frac{a}{2} (\partial_z V)^2 + \frac{bV^2}{2} + fV. \qquad (18)$$

The finite-element method is described in detail in Zienkiewicz (1967) and Oden and Carey (1983); only an outline is presented here. The region Ω is divided into N_E 2-D elements, and the kth element is defined by n(k) nodes with coordinates (y_i, z_i), $i = 1, \dots, n(k)$. The mesh contains N_n nodes in total. The solution, V approximated within each element by the nodal values v_i, $i = 1, \dots, n(k)$ and a set of shape functions ψ_i, $i = 1, \dots, n(k)$ in the kth element. V^k is given by

$$V^k(y, z) = \sum_{i=1}^{n(k)} v_i \psi_i(y, z). \qquad (19)$$

With this approximation for V, the Lagrangian (Clegg, 1989) can be simply expressed as a sum of integrals over individual elements,

$$\mathscr{L} = \sum_{k=1}^{N_E} \int^{\Omega_{Ek}} \left(\frac{a}{2} (\partial_y V)^2 + \frac{a}{2} (\partial_z V)^2 \right.$$

$$\left. + \frac{bV^2}{2} + Vf \right) dy \, dz, \qquad (20)$$

where Ω_{E_k} is the kth element. Substituting for V from equation (19), gives

$$\mathscr{L} = \sum_{k=1}^{N_E} \left[\int^{\Omega_E} \left(\frac{a}{2} (\Sigma v_j \partial_y \psi_j)^2 + \frac{a}{2} (\Sigma v_j \partial_z \psi_j)^2 \right. \right.$$

$$\left. \left. + \frac{b}{2} (\Sigma v_j \psi_j)^2 + f \Sigma v_j \psi_j \right) dy \, dz \right], \qquad (21)$$

where the inner sum extends from j = 1 to n(k). If the basis functions are required to have the property that

$$\psi_i = \delta_{ij} \text{ at } (y_j, z_j) \qquad (22)$$

at the nodal points y_i, z_i where $i, j = 1, \dots, n(k)$ and δ_{ij} is the Kronecker delta, then the contribution to $\mathscr{L}$ from each element can be conveniently written in quadratic form as

$$\mathscr{L}_E = \mathbf{v}_e^H \underline{\mathbf{K}}_e \mathbf{v}_e - \mathbf{v}_e^H \mathbf{f}_e, \qquad (23)$$

where $\mathbf{v}_e$ is the vector containing the node values and H denotes the conjugate transpose. The element stiffness matrix is given by

$$K_{ij} = \int^{\Omega_E} \left[\frac{a}{2} (\partial_y \psi_i)(\partial_y \psi_j) \right.$$

$$\left. + \frac{a}{2} (\partial_z \psi_i)(\partial_z \psi_j) + \frac{b}{2} \psi_i \psi_j \right] dy \, dz, \qquad (24)$$

where $i, j = 1, \dots, n(k)$ and $\mathbf{f}_e$ is the element load vector with components

$$F_i = \int^{\Omega_E} f \psi_i \, dy \, dz, \qquad (25)$$

where $i = 1, \dots, n(k)$. On summation over all elements the Lagrangian as in equation (24) can be written in the form

$$\mathscr{L} = \mathbf{v}^H \underline{\mathbf{K}} \mathbf{v} - \mathbf{v}^H \mathbf{f}, \qquad (26)$$

where $\mathbf{v} = [v_1, \dots, v_{N_n}]$ is the global solution vector of nodal values, $\underline{\mathbf{K}} = \sum_{i=1}^{N_e} \underline{\mathbf{K}}_e$ is the global stiffness matrix and $\mathbf{f} = \sum_{i=1}^{N_e} \mathbf{f}_e$ is the global load vector. K contains all of the information regarding the element sizes and media properties *(a and b)*, and v contains the unknown nodal values. To minimize $\mathscr{L}$ with respect to v, equation (26) is differentiated with respect to v and equated to zero, yielding the matrix equation, $\underline{\mathbf{K}}\mathbf{v} = \mathbf{f}$ which can be solved for v.

IMPLEMENTATION

Mesh generation

The success of a finite-element calculation depends on the way the solution region Ω is discretized into a finite-element mesh. The meshes used in this study have been generated with TRIMESH, a 2-D mesh generator described by Travis and Chave (1992) which permits a general triangular mesh (i.e., one composed of nonright triangles) to be produced from minimal input information and is capable of handling the most general of geometries, including multiply-connected regions. Figure 1 shows a typical mesh that was used in the seafloor examples described later in this paper. Since a general triangular mesh does not produce the simple banded matrix equation obtained when the mesh is com-
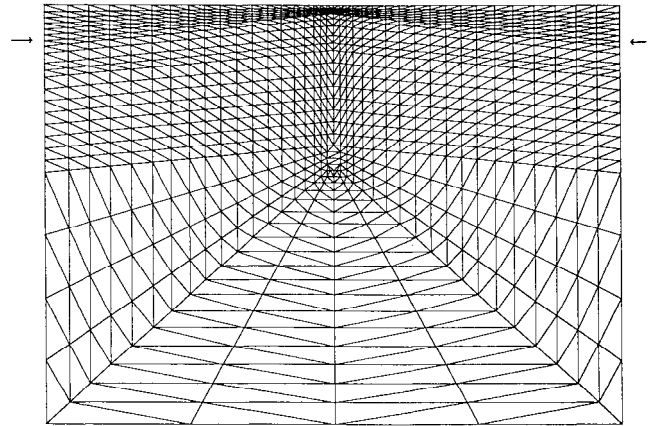

FIG. 1. A typical finite-element mesh used for modeling the fields of an HED source at the seafloor. The sloping seafloor is indicated by the arrows.

posed of right triangles, some matrix preprocessing to min-imize the bandwidth is required. The automatic node renum-bering algorithm of Collins (1973) is used to rearrange the matrix terms, hence optimally reducing the bandwidth by a factor of 100 or more. This allows efficient banded matrix solvers to be used to solve the finite-element equations.

Calculation of $\underline{\mathbf{K}}_E$ and $\mathbf{F}_E$

To express equations (13) and (14) in variational form, the integrals (24) and (25) must be evaluated. For general, isoparametric, triangular elements these integrals are ana-lytic, and the components of the element stiffness matrices and load vectors are derived in Appendix A.

Calculation of primary fields

Computation of the element load vectors at each wave-number requires that the three primary electric field compo-nents be evaluated at each node. If the primary conductivity structure is taken to be two half spaces, then the fields can be derived in closed form. The finite-element method will work for an arbitrary electromagnetic source, but this study con-centrates on the case of an infinitesimal horizontal electric dipole (HED). The primary fields for an HED were derived using a method similar to that of Chave and Cox (1982) and the expressions used are listed in Appendix B. The sine-cosine integrals were evaluated using a method similar to that described by Chave (1983) for Hankel transforms. Because the fields are spatially smooth, they may be calcu-lated at a reduced set of locations to save computation, with subsequent evaluations being obtained by spline interpola-tion.

Boundary conditions: Infinite elements

The electromagnetic fields obey a radiation condition at infinity; since the fields decay to zero at infinite distance from the source, imposing an essential boundary condition; i.e., forcing them to be zero at a finite range may result in significant errors. Extending the finite-element mesh to a distance of several skin depths requires many extra ele-ments, and the matrix equation rapidly becomes too large to be solved quickly or conveniently. Coggon (1971) and Prid-more et al. (1981) attempted to overcome this problem by terminating the mesh at natural boundaries so that no energy flowed across them. While such boundaries can be devised for the scattering problem in a whole space, this method cannot be used for the scattering due to a source near an interface, and some other way of modeling the dissipation of energy in all directions must be developed.

An elegant way to proceed is to apply a derivative boundary condition at a finite distance from the source. This requires that the solution V at the boundary satisfy

$$V + A(\nabla V) \cdot \mathbf{n} = B, \qquad (27)$$

where A and B are defined operators and n is the normal to the boundary. This is equivalent to extending the mesh to infinite distance from the source with a set of infinite elements. This type of element has been used extensively in other diffusive computational problems such as heat flow (Lewis et al., 1985). The geometry of one such element is

illustrated in Figure 2. The element has four nodes, and since two nodal values are set to zero, only two shape functions need be defined as

These shape functions are continuous with those in the adjoining triangular elements and allow the secondary fields to decay to zero with the appropriate decay constant, $\beta(z)$. To determine $\beta(z)$ it is often necessary to use a general technique such as that described in Pissanetzky (1983), but in the present instance the cylindrical symmetry of the secondary field can be used to find an approximate form. Thus for the horizontal elements on the right boundary of the mesh, the radial skin depth is resolved parallel to the element's infinite side to give,

$$\beta(z) = \beta_\rho \frac{y_E - y_s}{((y_E - y_s)^2 + z^2)^{1/2}}, \qquad (30)$$

where $\beta_\rho = (if\pi\mu_0\sigma_e)^{1/2}$, y_s is the horizontal coordinate of the source, f is its frequency, and σ_e is the conductivity of the infinite element. Similar expressions may be derived for the infinite elements on the left, top, and bottom sides of the mesh. The stiffness matrices and load vectors for the infinite elements are calculated in an identical manner to those for the triangular elements and are then added to the global matrix equation. The results are presented in Appendix C. The improvement made by using these elements is depicted in Figure 3, which shows the mean seafloor errors for the simple structure described in the section detailing the error
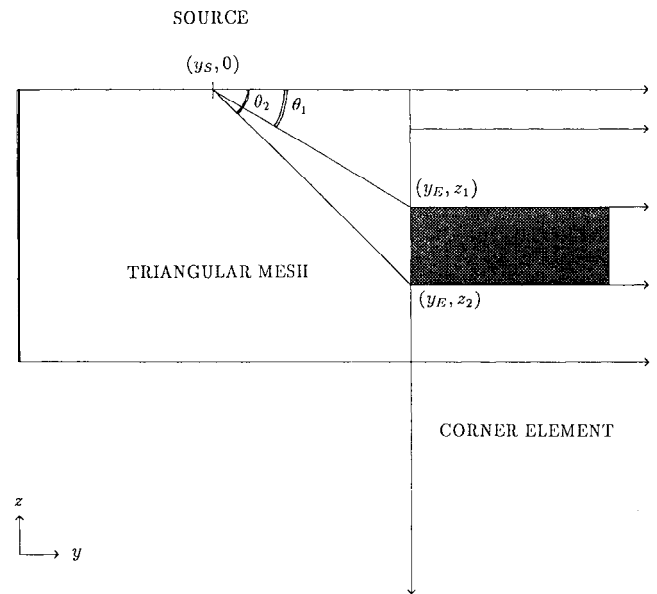

FIG. 2. The geometry of an infinite element in relation to the source.

analysis with both infinite elements and an essential bound-
ary condition implemented at 1.5 skin depths from the
source.

It remains to be shown that the use of infinite elements is
equivalent to applying a natural boundary condition at the
perimeter of the triangular mesh. In terms of node values and
shape functions,

$$V = (v_1\psi_1 + v_2\psi_2)e^{-\beta(y - y_E)}, \qquad (31)$$

and upon substitution into equation (27) at $y = y_E$, this
becomes

$$V - \beta(z)AV = B, \qquad (32)$$

which is satisfied for all z if $B = 0$ and $A = 1/\beta$.

Iterative solution of the coupled equations

As previously demonstrated in equations (13) and (14), at
least two electromagnetic field components are needed to
fully describe the physics of electromagnetic induction from
3-D sources, and it is convenient to solve for the along-strike
electric and magnetic field components. The other field
components can then be calculated by numerical differenti-
ation of these principal components using equations (7) to
(12). To avoid the errors arising from this process, both
Coggon (1971) and Lee and Morrison (1985) solved directly
for all three electric field components, but this approach
increases the size of the matrix equations by 50 percent.

The equations could be solved simultaneously for $\hat{E}_x^s$ and
$\hat{B}_x^s$, but this would double each dimension of the global
stiffness matrix and greatly increase the computer time and
memory needed for solution. It is more efficient to treat the
equations in an iterative fashion by including the coupling
terms on the right-hand sides of equations (13) and (14) in the
source term f. To do this $\hat{B}_x^s$ is set to zero and equation (13)
is solved for an initial $\hat{E}_x^s$. This is then used as a source term
in equation (14) to calculate $\hat{B}_x^s$ which is then used to
improve the approximation to $\hat{E}_x^s$. This cycle is repeated
until convergence is achieved, which is defined as occurring
when both the mean and maximum change in the secondary
fields at the earth's surface is less than some specified
amount. Figure 4 shows the number of iterations needed as
a function of wavenumber for a variety of convergence
parameters. The model used is the 1-D conductivity used in
the following section. This alternating solution is equivalent
to a minimization of the corresponding Lagrangian even
though the Lagrange density is never explicitly calculated.
Stoyer (1975) described a similar approximation scheme that
was unstable, possibly because the solution was for the total
fields. The present application appears to be the first suc-
cessful implementation of an iterative solution to this prob-
lem. Table 1 compares the performance of the iterative and
simultaneous solutions for $\hat{E}_x^s$ and $\hat{B}_x^s$ for meshes of varying
sizes on a Convex C-120 computer. The iterative solution is
particularly effective when meshes with more than 2000
nodes are being used. This is because these matrices are
close in size to the computer's memory, and it is quicker to
solve two matrices of order 2000 that will fit into memory at
one time than to solve one of order 4000 which does not. In
some instances it was necessary to damp the secondary
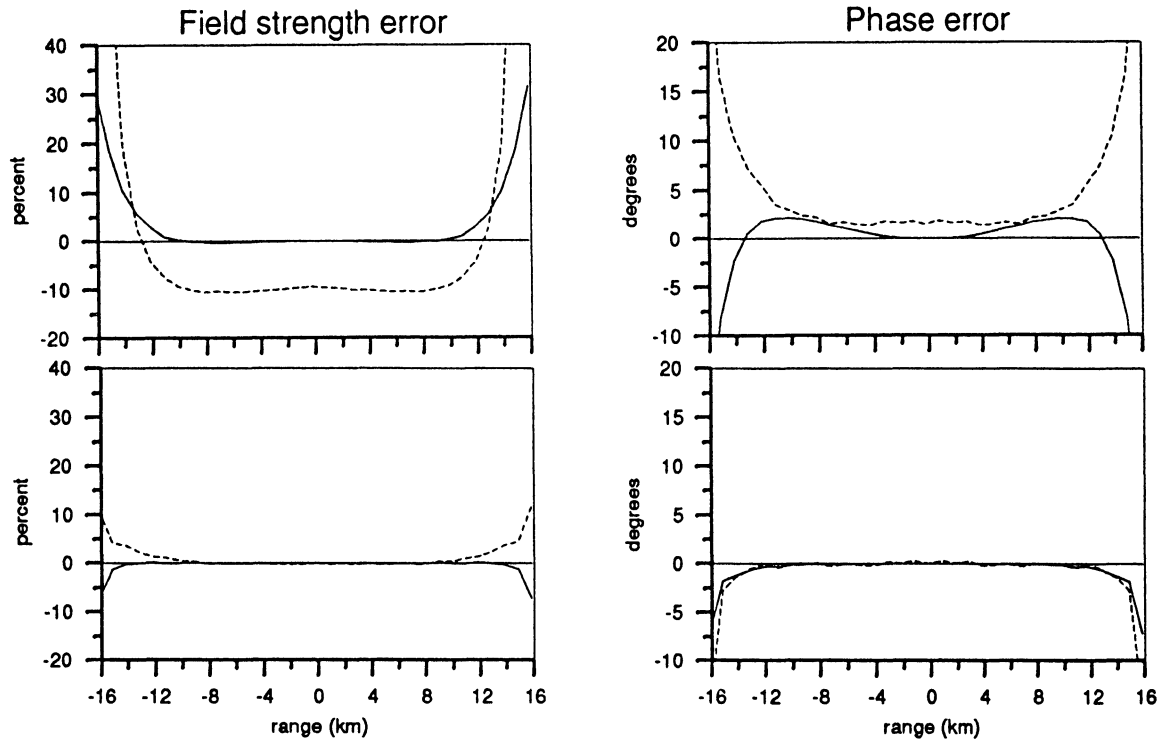

FIG. 3. Total and secondary field errors at the seafloor. The upper frame shows the errors that occur when the fields are forced
to zero at the edge of the mesh and the lower frames show the improvement obtained by using infinite elements. The dashed
line represents secondary field quantities and the solid line is for the corresponding total field quantities.

fields to ensure that the iteration does not diverge. The present algorithm automatically selects the value of a damping factor λ which lies between 0 and 1. If the field component at the previous iteration was $\hat{E}_{i-1}$ and at the present iteration is $\hat{E}_i$, then the damped value $\hat{E}_{damp}$ is defined as

$$\hat{E}_{damp} = \lambda \hat{E}_i + (1 - \lambda)\hat{E}_{i-1}. \qquad (33)$$

Inverse Fourier transform

Once the along-strike fields have been computed in the (k_x, y, z) domain at a discrete set of wavenumbers, inverse Fourier transforms,

$$E_x^s(x, y, z) = \frac{1}{2\pi} \int_{-\infty}^{\infty} dk_x e^{-ik_x x} \hat{E}_x^s(k_x, y, z), \quad (34)$$

$$B_x^s(x, y, z) = \frac{1}{2\pi} \int_{-\infty}^{\infty} dk_x e^{-ik_x x} \hat{B}_x^s(k_x, y, z) \qquad (35)$$

can be evaluated. Between wavenumbers, $\hat{B}_x^s$ and $\hat{E}_x^s$ are interpolated by cubic splines since both quantities are smooth functions of k_x. Figure 5 shows an example of $\hat{E}_x^s(k_x)$ at the seafloor for the structure used in the convergence study in the following section. With the current source parallel to the structure and located at ($x = 0$) $E_x^s(x, y, z)$ and $\hat{E}_x^s(k_x, y, z)$ are even functions of x and k_x, respec-

tively. Similarly, $B_x^s(x, y, z)$ and $\hat{B}_x^s(k_x, y, z)$ are odd functions of their respective variables for this orientation. Writing the exponential functions in terms of sines and cosines gives,

$$E_x^s(x, y, z) = \frac{1}{\pi} \int_0^{\infty} dk_x \cos(k_x x)\hat{E}_x^s(k_x, y, z) \qquad (36)$$

and

$$B_x^s(x, y, z) = -\frac{i}{\pi} \int_0^{\infty} dk_x \sin(k_x x)\hat{B}_x^s(k_x, y, z). \qquad (37)$$

Similar results are obtained when the source is perpendicular to strike, but with the symmetries reversed. The other secondary field components are evaluated by numerical differentiation of the along-strike field components. Finally, the primary fields of the point dipole are evaluated directly from Hankel transform expressions and added to equations (36) and (37) to yield the total electromagnetic fields.

VALIDATION OF THE CODE

It is vital to demonstrate that the results of a numerical method are accurate and independent of the parameterization. There are internal and external types of tests. External tests compare the results with alternative numerical methods or analytic results, while internal tests check for self-consistency and convergence with respect to the parameterization.

The parameterization of the 2.5-D problem is defined by the spatial parameterization-the mesh texture and extent-and the set of wavenumbers. The mesh texture is the number of elements per skin depth, and the mesh extent is the distance from the source that the triangular mesh extends before being terminated by infinite elements. In the wavenumber domain, the spacing of the wavenumber values at which the fields are computed and the upper and lower limits of the wavenumber spectrum must be specified. In both domains the finite-element solution becomes satisfactory when the linear finite elements or the polynomial spline functions become a good approximation to the quasi-exponentially decaying fields and when the parameterization extends over the appropriate range.

To demonstrate the accuracy of the method and to characterize its convergence, a simple 1-D model is used. The medium consists of two half-spaces with the lower one representing the earth ($\sigma = 0.003$ Sm^{-1}) and the upper one
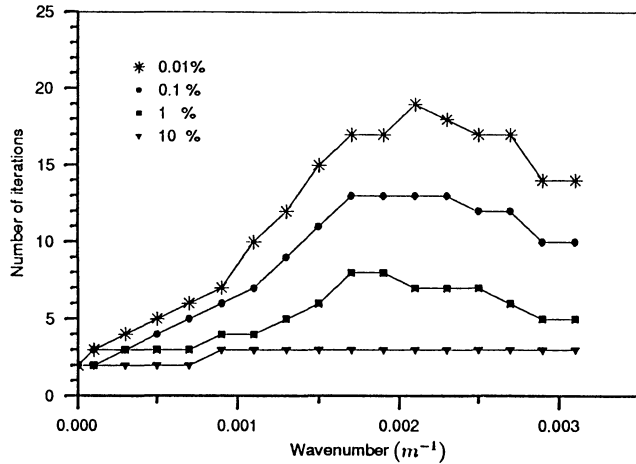

FIG. 4. Number of iterations required for convergence as a function of wavenumber for a range of termination parameters.

Table 1. Comparison of iterative and direct solution times in seconds for meshes with 2000, 1500, and 1000 nodes on a Convex C-120 computer.

Number of nodes	2000		1500		1000	
Solution method	Direct	Iterative	Direct	Iterative	Direct	Iterative
Forming matrix	220	6	70	4	4	3
Factorizing matrix	290	18	125	13	10	9
10 iterations	0	4	0	4	0	4
TOTAL	510	38	195	21	14	16

the seawater ($\sigma = 3.0 \, \text{Sm}^{-1}$). The source has a frequency of 8 Hz and is 20 m above the interface between the half-spaces. The lower half-space contains a 2 km thick conductive layer ($\sigma = 0.03 \, \text{Sm}^{-1}$) at a depth of 2 km. The seafloor fields computed with the 2.5-D finite-element method are compared with those obtained from the Hankel transform expressions of Chave and Cox (1982).

The accuracy of the seafloor fields with respect to the mesh texture M_t is shown in Figure 6. For a mesh with constant element spacing, the errors display a monotonic decrease as M_t increases, and with more than three elements per skin depth the change is small. It should be noted that at large wavenumbers the effective decay length d approaches $1/k_x$, which is shorter than that at zero wavenumber and independent of conductivity. Even though the mesh may only have one element per skin depth for these k_x-values, the spatial fields are still accurate since the high wavenumber terms make only a small contribution to the inverse Fourier transform. Lee and Morrison (1985) found it necessary to use a separate mesh for each wavenumber, but this has not been found to improve the present simulation. Meshes with textures varying with source range were also investigated and found to be capable of producing smaller errors around the source, but larger errors at the edge of the mesh when using the same number of nodes. The optimal mesh could be found by implementing a moving finite-element method, which has been shown in Travis and Chave (1991) to be useful in magnetotelluric modeling.
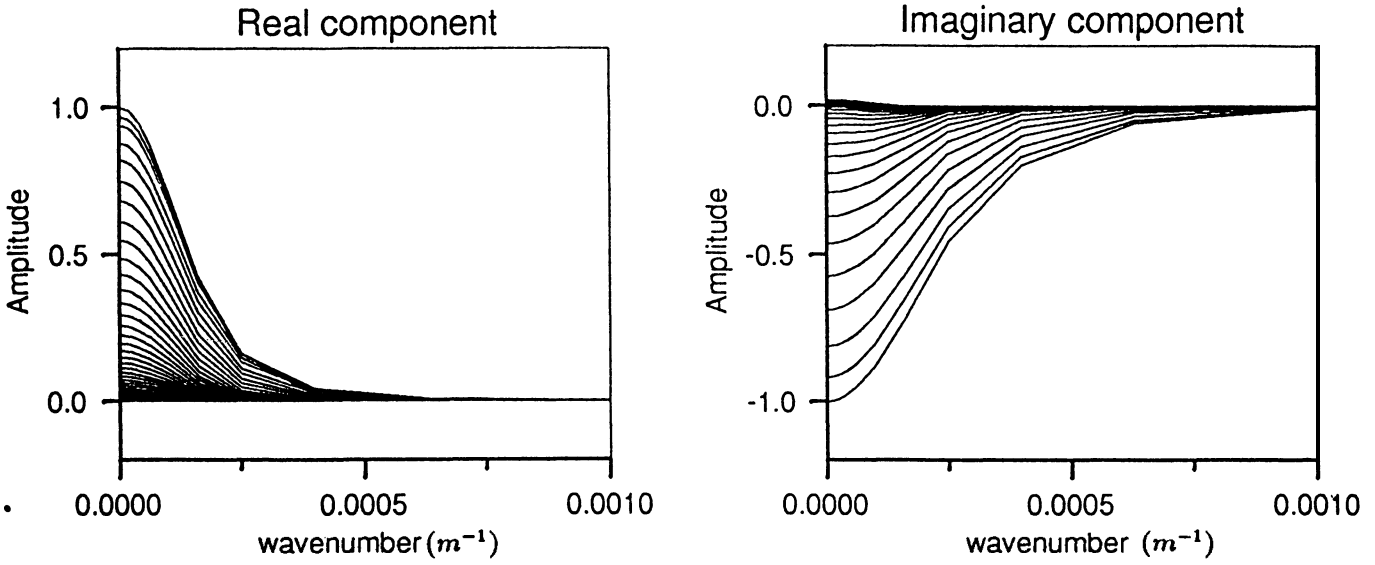

FIG. 5. Normalized real and imaginary components of $\hat{E}_x^s(k_x, y, z = 0)$ at the seafloor as a function of wavenumber for the conductivity structure used to validate the code. The curves with greatest amplitude are for points 500 m from the source, and subsequent curves are 500 m apart.
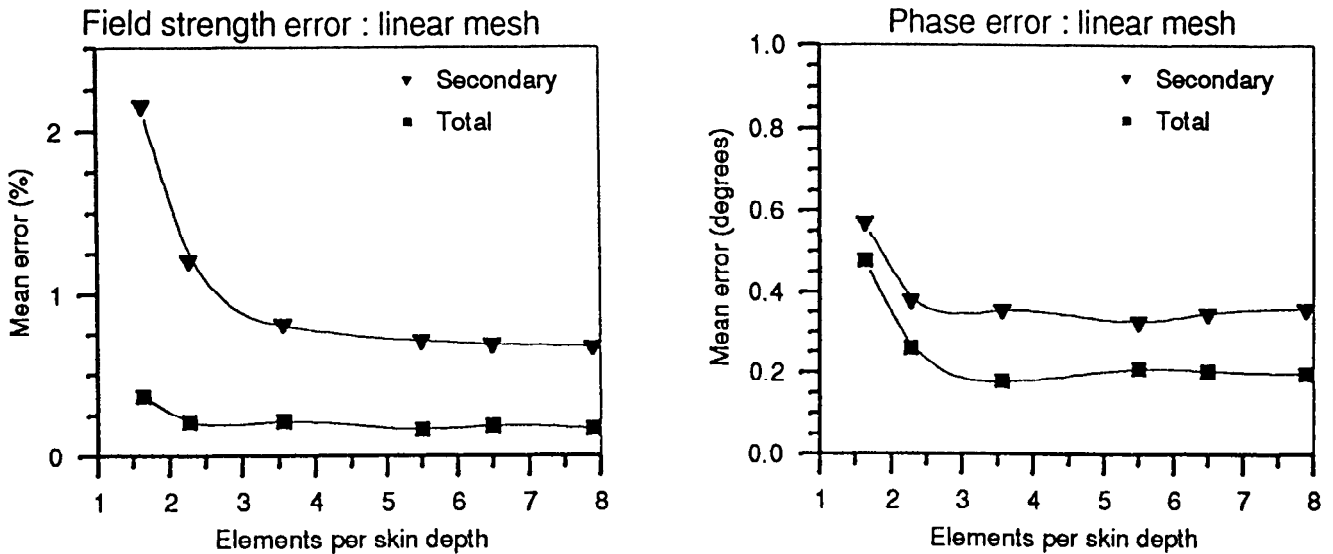

FIG. 6. Mean seafloor errors in the along-strike electric field as a function of the mesh texture.

Figure 7 shows the mean seafloor errors as a function of m_E, the mesh extent. Since the infinite elements represent the solution in the far-field, they cannot begin too close to the source, and it can be seen that $m_E = 1.5$ is generally adequate. With $m_E < 1.5$, the solution not only becomes inaccurate but the iterative solution may become unstable, since the infinite-element shape functions do not accurately approximate the secondary fields at less than a skin depth from the source. If an essential boundary condition were used instead of the infinite elements, then to obtain acceptable errors in the center of the mesh would require $m_E > 4$, which would increase the number of nodes needed by a factor of 3 and result in significantly more computation.

The fields in the wavenumber domain were represented by N_{kx} wavenumbers per decade and the dependence of the seafloor errors on this quantity are given in Figure 8. The errors show a very rapid decrease a N_{kx} is increased, and provided $N_{kx} > 5$, the wavenumber spectrum is adequately parameterized. The upper limit of the wavenumber spectrum, k_{max}, depends on R_{min}, the minimum distance from a region of nonzero $\Delta\sigma$ to the point at which the fields are required to have a specified accuracy. The fact that the fields have an increased high wavenumber content close to the source can be expressed as $R_{min} k_{max} = C$, where C is a constant of $0(1)$ as proposed in Snyder (1976). In this case, taking $C = 4$ and since $R_{min} = 2000$ m, this requires $k_{max} = 0.002$ m^{-1}. This is confirmed by Figure 9 which shows the monotonic decrease of the seafloor errors with respect to k_{max}. With a region of nonzero $\Delta\sigma$ close to the surface, many more k_x values must be included to accurately represent the fields in the Fourier domain, thus it is efficient to define the primary conductivity so as to maximize $Rmin$. This is achieved by allowing certain regions to have negative $\Delta\sigma$.

To accurately represent the fields at points along strike and not just in the plane of the dipole, it is necessary to define the minimum wavenumber k_{min} down to where there are N_{kx} wavenumbers per decade. This arises because at and along the strike range of X, the inverse Fourier transform must include wavelengths up to 2X and thus k_{min} is $O(\pi/X)$.

Using the criteria for a convergent parameterization outlined above, it was found empirically that for a typical problem 15 k_x values and up to 2000 nodes are required. The seafloor field strength and phase errors are shown in Figure 3, and everywhere are less than 5 percent and 2 degrees, respectively. They are largest at the mesh edge where the infinite-element approximation is least accurate. It is this behavior that produces the residual error at the highest parameterization in Figures 6 to 9.

Having demonstrated the accuracy of the code for 1-D conductivity structures, the code was applied to some simple 2-D structures. Unfortunately no solutions for an HED source have been published for a direct comparison of results. Thus a number of internal tests were applied to these 2-D solutions to ensure that they converged as the parameterization was progressively refined, and similar spatial and wavenumber requirements were obtained. Other internal tests have been used and indicate that the solutions are accurate and stable. For example, equation (1) requires that the divergence of the magnetic field should be zero, and since this condition is not imposed explicitly on the solution, it provides a good consistency check. The normalized divergence,

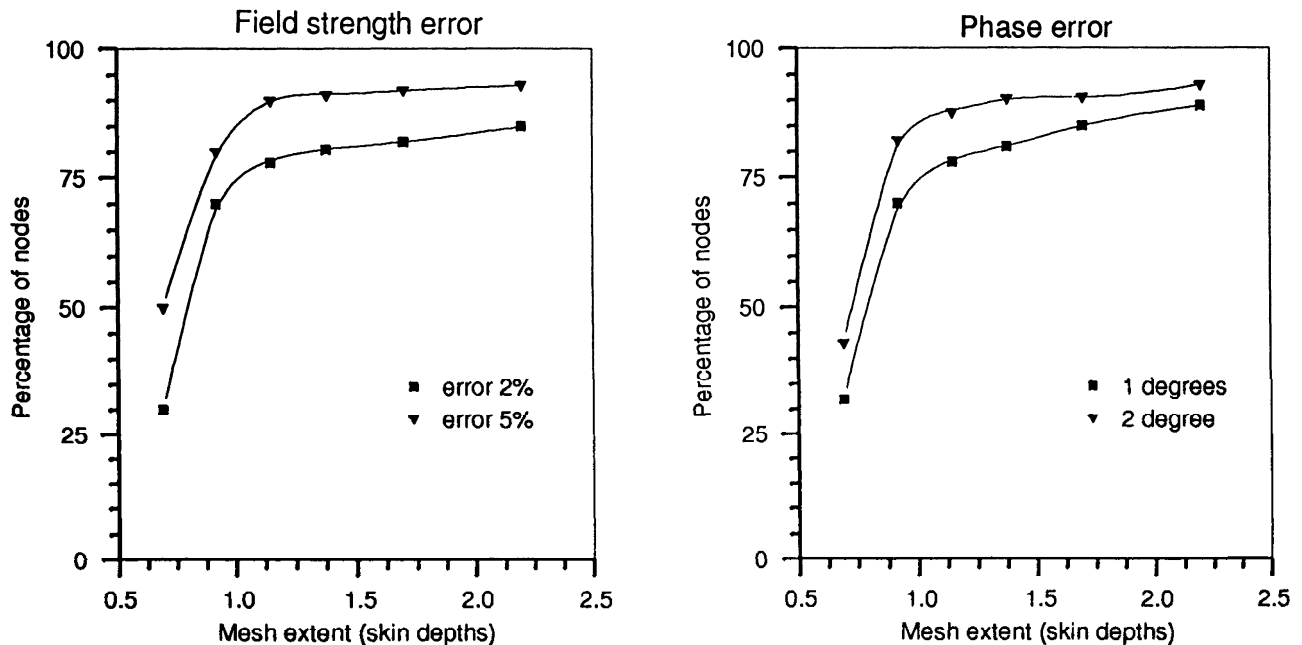$$\left(\frac{\partial_y B_y + \partial_z B_z}{\partial_y B_y - \partial_z B_z}\right), \tag{38}$$

FIG. 7. The percentage of seafloor nodes with secondary field strength and phase errors below a specified level as a function of mesh extent.

is generally in the range 10^{-4} to 10^{-6} indicating that this condition is well satisfied. Reciprocity is also a useful condition to consider (i.e., interchanging the source and receiver positions should result in the same fields at the receiver), and this is found to hold to within 2 percent and 2 degrees in the field strength and phases, respectively. The results in this section indicate that the solution is accurate to an acceptable degree and stable with respect to the spatial and wavenumber parameterization.

EXAMPLES

The code has been used extensively to simulate seafloor electromagnetic induction experiments using HED sources. The fields induced in the earth in such a configuration are very different from those produced in the terrestrial one since the earth is the least conductive region, rather than most conductive region, as is the case in terrestrial experimentation. Figures 10 and 11 show electric and magnetic
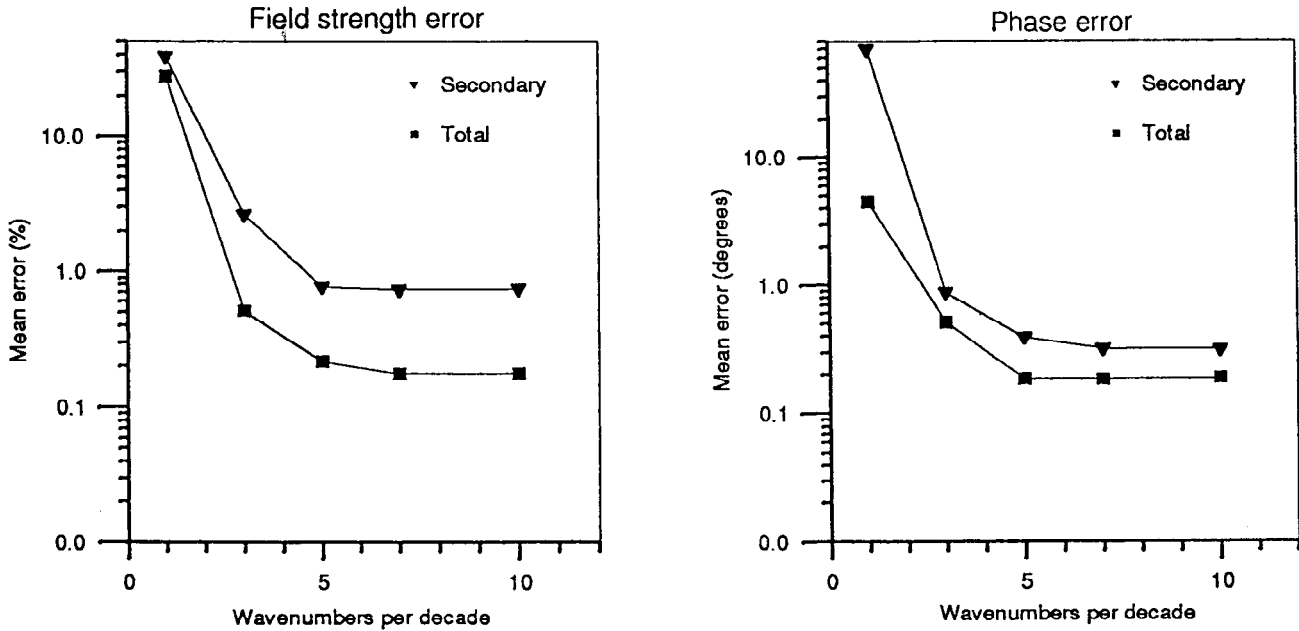
FIG. 8. Mean seafloor errors as a function of the number of k_x values per decade used to represent the fields in the Fourier domain.
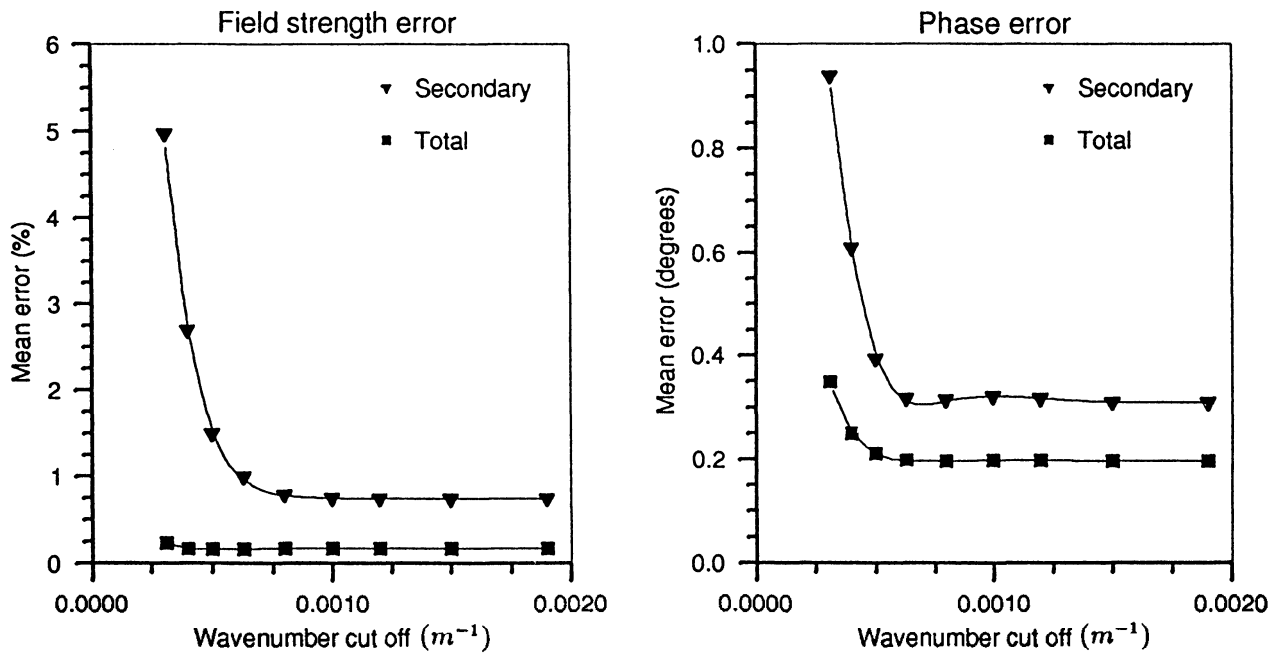
FIG. 9. Mean seafloor error as a function of the highest wavenumber used in the inverse Fourier transform.

field components of the fields that are induced in a uniform seafloor containing resistive and conductive prisms. In the former the HED source is parallel to the i-direction and thus, in a plane through the source only, E_x is nonzero. The current flow is predominantly parallel to conductivity gradients and thus the fields decay with length scales of the order of the skin depth, $d_c = (\sigma \mu_0 \pi f)^{1/2}$. The field strength and phase can be seen to vary more rapidly in the conductive seawater than in the resistive earth. The conductive prism can be seen to reduce the field strength and delay the phase, whereas the resistive prism has a minimal effect on the fields. In Figure I I the HED source is oriented in the j-direction, and in a plane through the source, the electromagnetic field is characterized by B_x. Two current vortices are generated, one above and one below the HED source. The one above the source produces a high flux density due to the tighter

circulation of current within the more conductive medium, but this high conductivity also acts to rapidly attenuate the electromagnetic fields. The vortex below is much more diffuse. Since current crosses conductivity gradients in this plane. the effect of the two prisms is markedly different to the previous example. Both produce a significant alteration of the current Row that is manifested in the magnitude and phase of B_x. In both of these orientations it can be seen that long range propagation of the fields produced by an HED source is dominantly through the more resistive half-space. Figure 12 shows a plan view of the seafloor in the vicinity of the HED source and demonstrates the 3-D nature of the electromagnetic fields induced in a 2-D earth by a point HED source. At zero along-strike range, the conductive prism reduces field strengths below their half-space values by simple attenuation, as was shown by the vertical section in
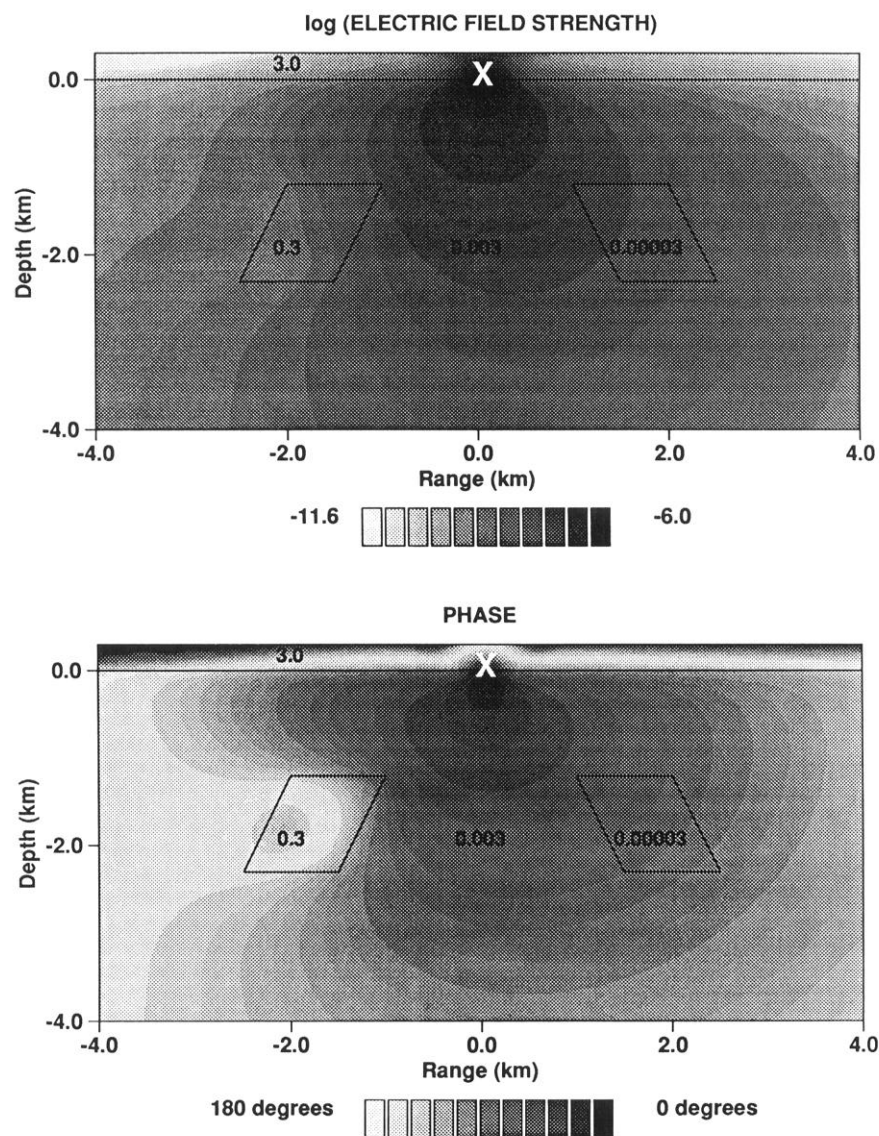

FIG. IO. Electromagnetic mode generated by an HED source at the seafloor parallel to i-direction with frequency of 1/2 Hz. Conductivities are in Sm^{-1} and the electric field strength is in Vm^{-1} per source dipole moment. The phase is relative to the source and mapped onto the interval 0 to 180 degrees. This results in 120 and 240 degrees appearing as the same shade, since they are both 60 degrees away from 180 degrees.

Figure 10. However at along-strike ranges greater than 2 km and above the conductive prism, the field strengths are increased above the half-space values by current channeling. Electric current that in a uniform half-space would turn at depths greater than 2 km is now able to take the low impedance path along the conductive prism. Thus the current density and hence electric field strengths are increased. Again, the resistive prism has minimal effect on the electromagnetic fields.

The code has also been applied to the case of an HED source at the earth-air interface. The fundamental difference with the previous example is that the 2-D conductivity structure is now contained within the more conductive half-space. The use of the primary-secondary separation, the iterative solution, and the infinite elements was again found to greatly reduce the computational requirements. The air is represented by a low but nonzero conductivity and

provided that the triangular mesh is extended at least 1.1 skin depths within it. the iterative solution was found to converge reliably. The infinite elements were found to be particularly effective in representing the fields in the air, since the conductivity contrast between the earth and air is greater than that between the earth and seawater in the previous example. The response of uniform earth containing a conductive prism is shown in Figure 13. Note that the conductive body attenuates signals traveling through the earth so that signals received at ranges of more than a kilometer to the right of the source are dominated by electromagnetic energy that has propagated through the air. As expected these signals have larger field strengths and earlier phases. Since the electromagnetic fields' propagation is dominantly through the air, such a survey would be relatively insensitive to earth conductivity more than a skin depth below the surface of the earth.
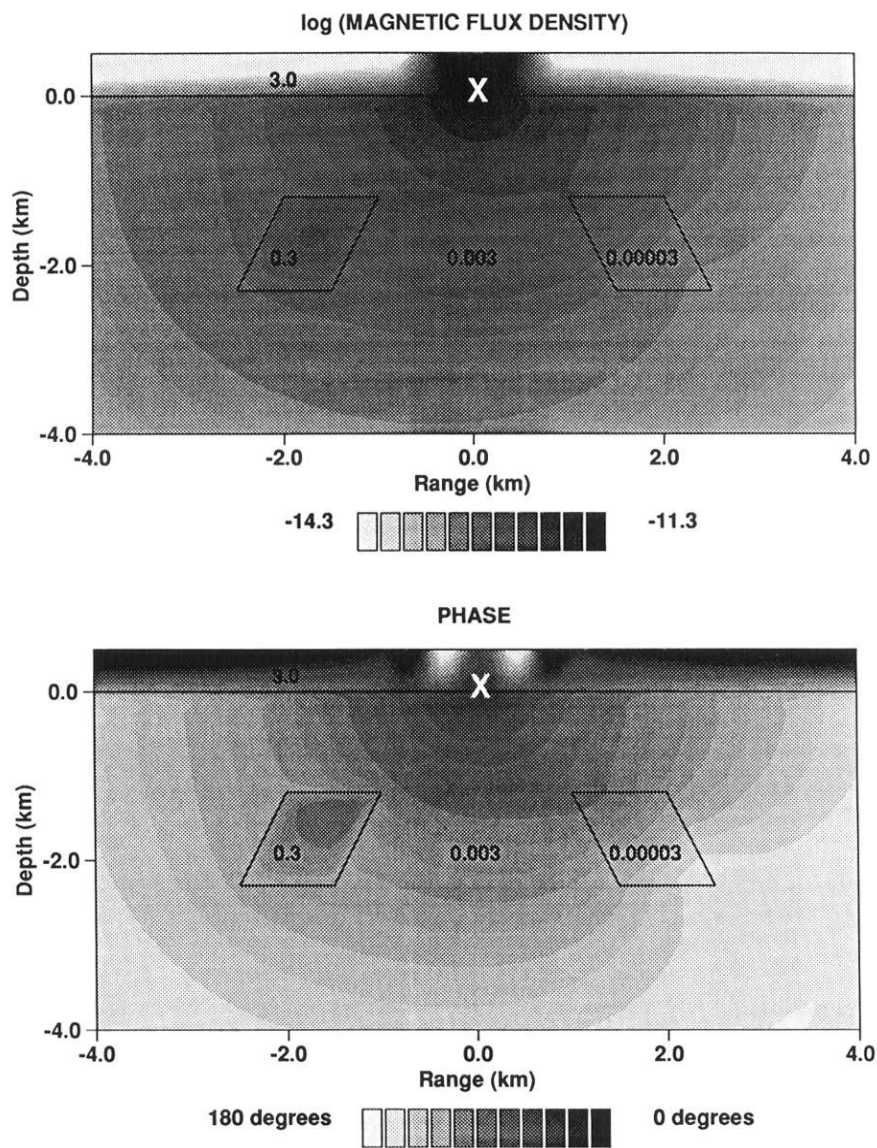

FIG. 11. Electromagnetic mode generated by an HED source at the seafloor normal to x-direction with frequency of 1/2 Hz. Conductivities are in Sm^{-1} and the magnetic flux density is in *Tper* source dipole moment. The phase is relative to the source and mapped on to the interval 0 to 180 degrees.

CONCLUSIONS

The 2.5-D numerical method described in this paper has been found to be useful for simulating electromagnetic induction experiments. The combination of the secondary field iterative solution with the use of infinite elements has considerably reduced the computational cost. Both execution time and memory requirements have been reduced by more than a factor of 10 compared to solutions not using these features. In conjunction with the use of a general triangular mesh the method permits the response of complex conductivity models to be computed with ease. It is stable for both terrestrial and marine applications, but becomes particularly efficient for the latter since the rapid decay of secondary fields with the conductive seawater layer allows the mesh to be terminated very close to the seafloor, thus greatly reducing the number of elements required to represent the electromagnetic fields.

The performance and applicability of the algorithm could be further improved. Quadratic elements could be used along internal boundaries between regions of differing conductivity to explicitly allow the continuity of normal electric current and magnetic flux density to be imposed. At high wavenumbers the electromagnetic fields in the Fourier domain become independent of conductivity and decay as

$$\hat{E}(r) = \hat{E}_0 \exp(-k_x r), \qquad (39)$$

where r is the radial distance from the source and $\hat{E}_0$ is a constant. Thus $\hat{E}(r)$ will develop a spatial singularity and be poorly represented by the finite elements. This wavenumber singularity could be subtracted from the secondary fields in a manner analogous to the primary-secondary separation used to remove the spatial singularity of the source. This is generally unnecessary unless the solution near the source is of interest. The applicability of the code could be increased
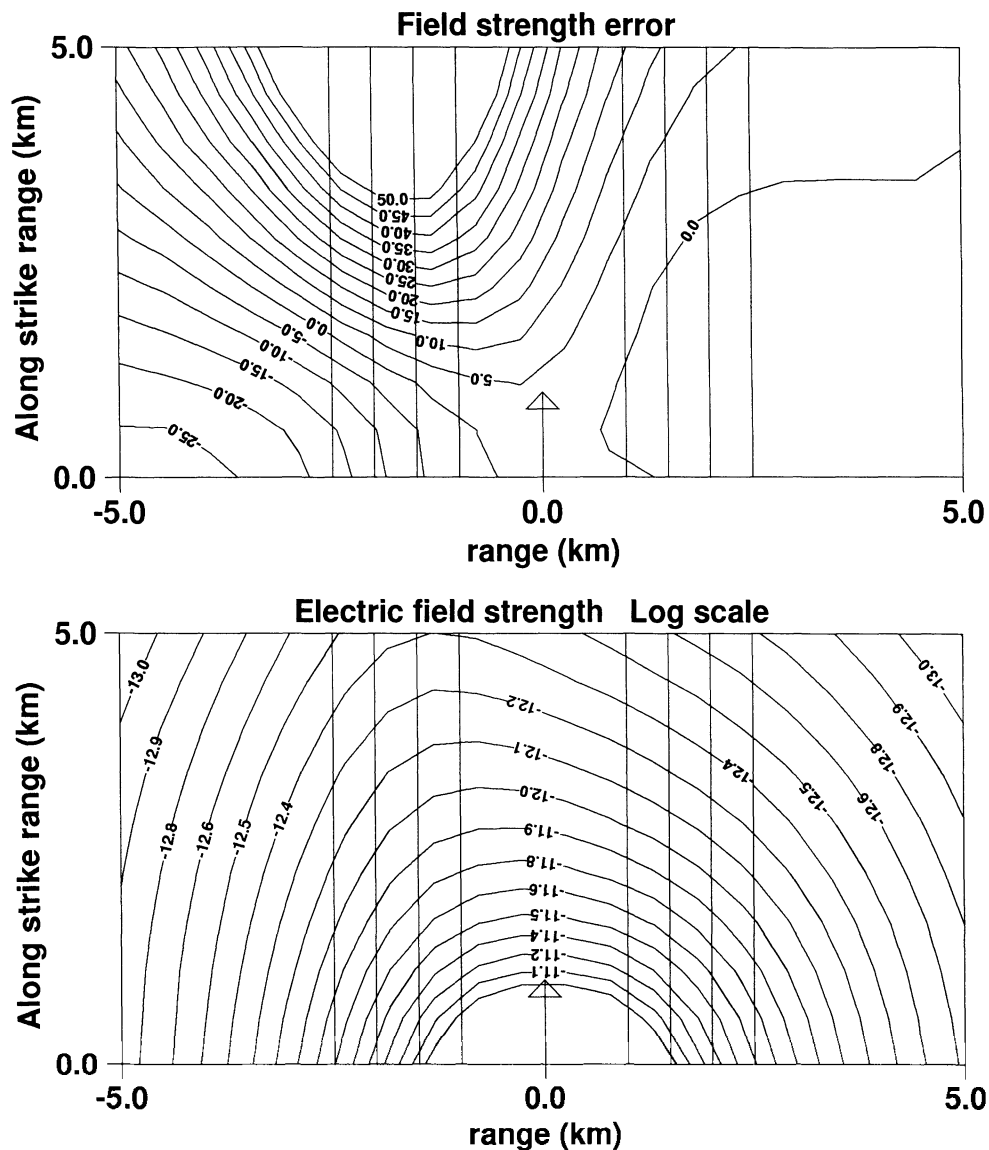

FIG. 12. A plan view of the (x, y) plane (the seafloor) showing the along strike field variations produced by the 2-D structure shown in Figure 10. The source orientation is shown by the arrow and the position of the prisms is indicated by the straight lines.
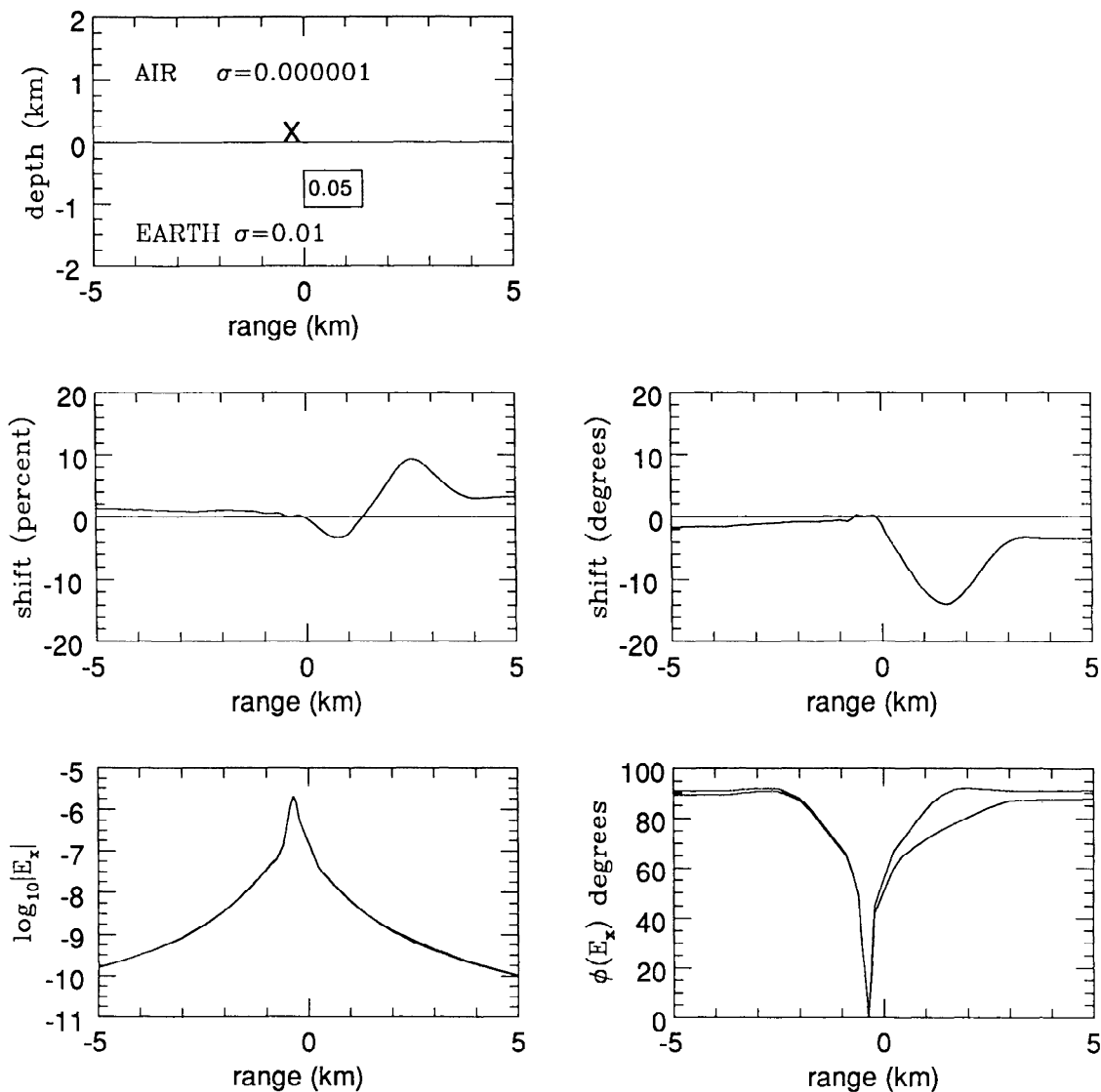
FIG. 13. Electromagnetic fields at the earth's surface generated by a HED source marked "X" with frequency 100 Hz over the conductivity model shown in the upper panel. The source is parallel to the invariant conductivity direction. All conductivities are in Sm^{-1}. The shifts in the fields are relative to those computed for a double half-space model.

by considering other types of finite-electromagnetic sources. The features that have improved the performance in the present application (infinite elements and the iterative solution) are expected to produce comparable improvements in modeling of the fields generated by other types of electromagnetic source.

REFERENCES

Chave, A. D., 1983, Numerical integration of related Hankel transforms by quadrature and continued fraction expansion: Geophysics, 48, 1671-1686.

Chave, A. D., and Cox, C. S., 1982, Controlled electromagnetic sources for measuring electrical conductivity beneath the oceans, Part I, Forward problem and model study: J. Geophys. Res., 88, 5327-5338.
Clegg, J. C., 1968, Calculus of variation: Oliver & Boyd.
Coggon, J. H., 197 1, Electromagnetic and electrical modeling by the finite-element method: Geophysics, 36, 132-155.
Collins, R. J., 1973, Bandwidth reduction by automatic renumbering: Int. J. for Numer. Meth. in Eng., 6, 345-356.
Everett, M. E., 1990, Mid-ocean ridge electromagnetics: Ph.D. thesis, University of Toronto.
Fox, R. C., Hohmann, G. W., Killpack, J. J., and L. Rijo, 1980, Topographic effects in resistivity and induced polarization surveys: Geophysics, 45, 75-93.
Lee, K. H., 1978, Electromagnetic scattering by a two-dimensional inhomogeneity due to an oscillating magnetic dipole source: Ph.D. thesis, Univ. of California, Berkeley.
Lee, K. H., and Morrison, H. F., 1985, A numerical solution for the electromagnetic scattering by a two-dimensional inhomogeneity: Geophysics, 50, 1163-l 165.
Lewis, R. W., Morgan, K., and Roberts, P. M., 1985, Infinite-element modeling of heat loss during thermal recovery processes: Soc. Petr. Expl. Res. Symp.

Moghaddam, M., Yannakakis, E. J., Chew, W. C., and Randall, R., 1991, Modeling of the subsurface interface radar: J. Elect. Waves and Appl., 5, 17-39.

Oden, J. T., and G. F. Carey, 1983, An introduction to the finite-element method: Prentice-Hall, Inc.

Pissanetzky, S., 1983, An infinite element and a formula for numerical quadrature over an infinite interval: Int. J. for Num. Meth. in Eng., 19, 913-927.

Pridmore, D. F., Hohmann, G. W., and Ward, S. H., 1981, An investigation of finite-element modeling for electric and electromagnetic data in three dimensions: Geophysics, 46, 1009-1024.

Snyder, D. D., 1976, A method for modeling the resistivity and induced polarization response of two-dimensional bodies: Geophysics, 41, 997-1015.

Stoyer, C. H., 1975, Numerical solutions of the response of a 2-D earth to an oscillating magnetic dipole source with applications to a ground water study: Ph.D. thesis, Pennsylvania State Univ.

Stoyer, C. H., and Greenfield, R. J., 1976, Numerical solutions of the response of a two-dimensional earth to an oscillating magnetic dipole source: Geophysics, 41, 519-530.

Travis, B. J., and Chave, A. D., 1989, A moving finite-element method for magnetotelluric modeling: Phys. Earth Planet. Int., 53, 432-443.

Zienkowicz, O. C., 1967, The finite-element method in structural and continuum mechanics: McGraw Hill Book Co.

APPENDIX A
ELEMENT STIFFNESS MATRICES AND LOAD VECTORS

With a triangular element having nodes at y_i, z_i, $i = 1, \ldots$) 3 the diagonal and off-diagonal terms of the element stiffness matrix are of the form,

$$K_{11} = \frac{1}{2J}\left[a((y_3 - y_2)^2 + (z_3 - z_2)^2) + \frac{b}{12}\right], \quad \text{(A-1)}$$

$$K_{12} = \frac{1}{2J}\left[a((y_1 - y_3)(y_3 - y_2)\right.$$

$$\left. + (z_1 - z_3)(z_3 - z_2)) + \frac{b}{24}\right], \quad \text{(A-2)}$$

where

$$J = \frac{1}{|(z_3 - z_1)(y_2 - y_1) - (y_3 - y_1)(z_2 - z_1)|} \quad \text{(A-3)}$$

and the other matrix elements may be obtained by cyclic permutation of the indices. Thus, for equation (13) $a = \mu_0\sigma/\gamma^2$ and $b = \mu_0\sigma$, and for equation (14) $a = i\omega/\gamma^2$ and $b = i\omega$. The source term of equation (13) is of the form

$$f = \mu_0\Delta\sigma\hat{E}_x^p - ik_x\nabla\cdot\left(\frac{\Delta\sigma\hat{E}^p}{\gamma^2}\right) + ik_x\left[\nabla\hat{B}_x^s \wedge \nabla\left(\frac{1}{\gamma^2}\right)\right]\cdot\hat{x}$$

$$\text{(A-4)}$$

$$= f^a \quad + f^b \quad + f^c. \quad \text{(A-5)}$$

The three terms f^a, f^b, and f^c are considered in turn, and thus the first component of the element load vector may be written as $F_1 = F_1^a + F_1^b + F_1^c$. In each element the primary and secondary electric and magnetic field components are expressed in terms of their nodal values $\hat{E}_{xi}^p$, $\hat{E}_{yi}^p$, $\hat{E}_{zi}^p$, $\hat{E}_{xi}^s$, $\hat{B}_{xi}^s$ with $i = 1, \ldots, 3$, and thus

$$F_i^a = \int \psi_i\mu_0\Delta\sigma\hat{E}_x^p \, dA$$

$$= -\frac{\mu_0\Delta\sigma}{24J}(2\hat{E}_{xi}^p + \hat{E}_{x(i+1)}^p + \hat{E}_{x(i+2)}^p), \quad \text{(A-6)}$$

where $i = 1, \ldots, 3$. The second term contributes

$$F_i^b = ik_x\int \nabla\cdot\psi_i\left(\frac{\mu_0\Delta\sigma\hat{E}^p}{\gamma^2}\right) dA \quad \text{(A-7)}$$

to the element load vector where $i = 1, \ldots, 3$, and since $\Delta\sigma/\gamma^2$ is discontinuous at the element boundaries, it contains singularities. To perform the integration, the vector identity

$$\nabla(a\mathbf{b}) - a\nabla\cdot\mathbf{b} + \mathbf{b}\cdot\nabla a \quad \text{(A-8)}$$

is used where a is a scalar and $\mathbf{b}$ is a vector, giving the result

$$F_i^b = ik_x\int\left[\nabla\cdot\left(\frac{\psi_i\mu_0\Delta\sigma\hat{E}^p}{\gamma^2}\right) - \frac{\mu_0\Delta\sigma\hat{E}^p\cdot\nabla\psi_i}{\gamma^2}\right] dA,$$

$$\text{(A-9)}$$

where $i = 1, \ldots, 3$. From Green's theorem in the plane, the first term in equation (A-9) reduces to

$$ik_x\oint_{\partial\Omega}\frac{\psi_i\mu_0\Delta\sigma\hat{E}^p\cdot\hat{n}}{\gamma^2} dA, \quad \text{(A-10)}$$

where $\Delta\sigma/\gamma^2$ is constant within each element, but undefined at the interface. If the value on the interface is defined to be the arithmetic mean of the value in the two elements, summation over all elements of the line integral terms will cancel when all of the elements are considered. Thus, ignoring these line integral terms, the first component of the element load vector becomes

$$F_1^b = \frac{ik_x\mu_0\Delta\sigma}{6\gamma^2|J|}[(z_2 - z_3)(\hat{E}_{y1}^p + \hat{E}_{y2}^p + \hat{E}_{y3}^p)$$

$$- (y_2 - y_3)(\hat{E}_{z1}^p + \hat{E}_{z2}^p + \hat{E}_{z3}^p)]. \quad \text{(A-11)}$$

and the others may be obtained by cyclic permutation of the indices. The coupling term, f^c, contributes

$$F_i^c = ik_x\int_\Omega \psi_i\left[\nabla\hat{B}_x^s \wedge \nabla\left(\frac{1}{\gamma^2}\right)\right]\cdot\hat{x} \, dA \quad \text{(A-12)}$$

to the element load vector, where $i = 1, \ldots, 3$. This integral also contains terms that are singular at element boundaries, and the identity

$$\nabla\wedge(a\mathbf{b}) - a\nabla\wedge\mathbf{b} - \mathbf{b}\wedge\nabla a \quad \text{(A-13)}$$

is used to show that

$$ik_x \int \psi_i \nabla \hat{B}^s_x \wedge \nabla \left(\frac{1}{\gamma^2} \right) dA = ik_x \int \left[\frac{1}{\gamma^2} \nabla \wedge (\psi_i \nabla \hat{B}^s_x) \right.$$

$$\left. - \nabla \wedge \left(\frac{\nabla \hat{B}^s_x}{\gamma^2} \right) \right] dA \quad (A-14)$$

where $i = 1, \ldots, 3$. Using Stokes's theorem, the second area integral reduces to a line integral yielding

$$F^c_i = ik_x \int \frac{1}{\gamma^2} \nabla \wedge (\psi_i \nabla \hat{B}^s_x)\, dA - ik_x \oint \frac{\psi_i \nabla \hat{B}^s_x}{\gamma^2} \cdot \mathbf{dl}. \quad (A-15)$$

Again, the line integral terms cancel when all the elements are considered, and the contribution to the first component of the element load vector can be written in the form,

$$F^c_1 = \frac{ik_x \hat{B}^s_{x2}}{2|J|\gamma^2} [(x_1 - x_3)(y_2 - y_3) - (y_3 - y_1)(x_3 - x_1)]$$

$$+ \frac{ik_x \hat{B}^s_{x3}}{2|J|\gamma^2} [(x_2 - x_1)(y_2 - y_3) - (y_1 - y_2)(x_3 - x_2)] \quad (A-16)$$

with the other components being obtained by a cyclic permutation of the indices.

The element load vector for equation (14) is calculated in an almost identical manner with $f = f^d + f^e$. The first term,

$$f_d = i\omega\mu_0 \nabla \wedge \left(\frac{\Delta\sigma\hat{E}^p}{\gamma^2} \right) \cdot \hat{x} + ik_x \left[\nabla \hat{B}^s_x \wedge \nabla \left(\frac{1}{\gamma^2} \right) \right] \cdot \hat{x} \quad (A-17)$$

contributes

$$F^d_i = i\omega\mu_0 \int^\Omega \psi_i \nabla \wedge \left(\frac{\Delta\sigma\hat{E}^p}{\gamma^2} \right) dA, \quad (A-18)$$

where $i = 1, \ldots, 3$ to the element load vector. Using the identity (A-13) and Stokes's theorem, it is straightforward to show that for a triangular element the contribution to the first component of the element load vector is of the form

$$F^d_1 = \frac{i\omega\Delta\sigma\mu_0}{J\gamma^2} [(z_2 - z_3)(\hat{E}^p_{z1} + \hat{E}^p_{z2} + \hat{E}^p_{z3})$$

$$+ (y_2 - y_3)(\hat{E}^p_{y1} + \hat{E}^p_{y2} + \hat{E}^p_{y3})], \quad (A-19)$$

and the others are obtained by cyclic permutation of the indices. The contribution from the coupling term f^e is given by,

$$F^e_1 = \frac{ik_x \hat{E}^s_{x2}}{2|J|\gamma^2} [(y_1 - y_3)(z_2 - z_3) - (z_3 - z_1)(y_3 - y_1)]$$

$$+ \frac{ik_x \hat{E}^s_{x3}}{2|J|\gamma^2} [(y_2 - y_1)(z_2 - z_3) - (z_1 - z_2)(y_3 - y_2)], \quad (A-20)$$

and again the other components are obtained by a cyclic permutation of the indices.

APPENDIX B
PRIMARY FIELDS FOR AN HED SOURCE IN THE (k_x, y, z) DOMAIN

The simplest primary conductivity structure consists of two half-spaces having conductivities σ_0 and σ_1 with a dipole source parallel to the t-direction and at a height z' above the interface. In the half-space containing the source $(z > 0)$ the fields at a point (k_x, y, z)

$$\hat{E}_x = -\frac{\mu_0 p}{\pi\sigma_0} \int_0^\infty \frac{\cos(k_y y)}{2\beta_0(k_x^2 + k_y^2)} [(\lambda_0^2 k_y^2 + k_x^2\beta_0^2)e^{-\beta_0|z - z'|}$$

$$+ (R_L^{PM}\lambda_0^2 k_y^2 - R_L^{TM}k_x^2\beta_0^2)e^{-\beta_0(z + z')}]\, dk_y, \quad (B-1)$$

$$\hat{E}_y = \frac{\mu_0 p}{\pi\sigma_0} \int_0^\infty \frac{k_x k_y \sin(k_y y)}{2\beta_0(k_x^2 + k_y^2)} [(\beta_0^2 - \lambda_0^2)e^{-\beta_0|z - z'|}$$

$$- (R_L^{PM}\lambda_0^2 - R_L^{TM}\beta_0^2)e^{-\beta_0(z + z')}]\, dk_y, \quad (B-2)$$

$$\hat{E}_z = -\frac{\mu_0 p k_x}{2\pi\sigma_0} \int_0^\infty \cos(k_y y)[\pm e^{-\beta_0|z - z'|}$$

$$+ R_L^{TM}e^{-\beta_0(z + z')}]\, dk_y \quad (B-3)$$

and

$$\hat{B}_x = \frac{ip\mu_0 k_x}{\pi} \int_0^\infty \frac{k_y \sin(k_y y)}{k_x^2 + k_y^2}$$

$$\times (R_L^{PM} + R_L^{TM})e^{-\beta_0(z + z')}\, dk_y. \quad (B-4)$$

And in the source-free half-space $(z < 0)$ these expressions become,

$$\hat{E}_x = -\frac{\mu_0 p}{\pi\sigma_1} \int_0^\infty \frac{\cos(k_y y)e^{-(\beta_0 z' - \beta_1 z)}}{2\beta_0(k_x^2 + k_y^2)}$$

$$\times [\lambda_1^2 k_y^2(1 + R_L^{PM}) + k_x^2\beta_0\beta_1(1 - R_L^{TM})]\, dk_y, \quad (B-5)$$

$$\hat{E}_y = \frac{\mu_0 p}{\pi\sigma_1} \int_0^\infty \frac{k_x k_y \sin(k_y y)e^{-(\beta_0 z' - \beta_1 z)}}{2\beta_0(k_x^2 + k_y^2)}$$

$$\times [-\lambda_1^2(1 + R_L^{PM}) + \beta_0\beta_1(1 - R_L^{TM})]\, dk_y, \quad (B-6)$$

$$\hat{E}_z = -\frac{\mu_0 p k_x}{2\pi\sigma_1} \int_0^\infty \cos(k_y y)e^{-(\beta_0 z' - \beta_1 z)}(1 - R_L^{TM})\, dk_y, \quad (B-7)$$

and

$$\hat{B}_x = \frac{ip\mu_0 k_x}{2\pi} \int_0^\infty \frac{k_y \sin(k_y y)}{\beta_0(k_x^2 + k_y^2)}$$

$$\times e^{-(\beta_0 z' - \beta_1 z)}[R_L^{PM} + R_L^{TM}]\, dk_y, \qquad \text{(B-8)}$$

where the complex reflection coefficients are

$$R_L^{PM} = \frac{\beta_0 - \beta_1}{\beta_0 + \beta_1} \text{ and } R_L^{TM} = \frac{\sigma_1\beta_0 - \beta_1\sigma_0}{\sigma_1\beta_0 + \beta_1\sigma_0}, \qquad \text{(B-9)}$$

with $\lambda_0^2 = -i\omega\mu_0\sigma_0$, $\lambda_1^2 = -i\omega\mu_0\sigma_1$, $\beta_0^2 = k_x^2 + k_y^2 + \lambda_0^2$, $\beta_1^2 = k_x^2 + k_y^2 + \lambda_1^2$ and the upper sign in equation (B-4) is for $z > z'$. Very similar expressions can be obtained when the dipole is parallel to the $\hat{y}$-direction.

APPENDIX C

STIFFNESS MATRIX AND LOAD VECTORS FOR INFINITE ELEMENTS

The element stiffness matrices and load vectors for the infinite elements are calculated from integrals (24) and (25) in an identical manner to those for the triangular elements. The function $\beta(z)$ defined in equation (30) is approximated to the constant value at each node, and for the rectangular infinite element of width Δz shown in Figure 5, the shape functions are

$$\psi_1 = \frac{(z - z_2)}{(z_1 - z_2)} e^{\beta_1(y - y_2)} \text{ and } \psi_2 = \frac{(z_1 - z)}{(z_1 - z_2)} e^{\beta_2(y - y_2)}, \qquad \text{(C-1)}$$

where

$$\beta_1 = \cos\theta_1 \sqrt{k_x^2 - i\omega\mu_0\sigma} \text{ and } \beta_2 = \cos\theta_2\sqrt{k_x^2 - i\omega\mu_0\sigma}, \qquad \text{(C-2)}$$

and θ_1 and θ_2 are defined in Figure 2. To represent the primary fields in terms of the shape functions it is necessary to define their decay constants as

$$\beta_1^p = \cos\theta_1 \sqrt{k_x^2 - i\omega\mu_0\sigma_p} \text{ and } \beta_2^p = \cos\theta_2 \sqrt{k_x^2 - i\omega\mu_0\sigma_p}, \qquad \text{(C-3)}$$

where σ_p is the primary conductivity of the element. In the corners a half-infinite square element is used with a single shape function of the form

$$\psi_c = e^{-(\beta_z z + \beta_y y)}, \qquad \text{(C-4)}$$

where β_y and β_z are the decay constants resolved in the $\hat{y}$- and Z-directions, respectively. The results in the following section are for an element on the right-hand side of the mesh, and the expressions for the other sides can be derived in a similar way provided that care is taken to ensure that the primary field components are interchanged, since in these elements the i-component of the primary field is parallel, rather than normal to the strip. The elements of the symmetric 2 X 2 stiffness matrix are

$$K_{11} = a\left(\frac{\beta_1\Delta z}{6} + \frac{1}{2\beta_1\Delta z}\right) + \frac{b\Delta z}{6\beta_1},$$

$$K_{22} = a\left(\frac{\beta_2\Delta z}{6} + \frac{1}{2\beta_2\Delta z}\right) + \frac{b\Delta z}{6\beta_2} \qquad \text{(C-5)}$$

$$K_{12} = a\left(\frac{\beta_1\beta_2\Delta z}{6(\beta_1 + \beta_2)} - \frac{1}{(\beta_1 + \beta_2)\Delta z}\right) + \frac{b\Delta z}{3(\beta_1 + \beta_2)}. \qquad \text{(C-6)}$$

For the corner elements the matrix has a single element of the form

$$K_{11} = \frac{a(\beta_y^2 + \beta_z^2) + b}{4\beta_y\beta_z}. \qquad \text{(C-7)}$$

For equation (13) $a = \mu_0\sigma/\gamma^2$ and $b = \mu_0\sigma$ and for the along-strike magnetic field equation (14), $a = i\omega/\gamma^2$ and $b = i\omega$.

Separating the source terms into the five functions $f_a - f_e$ defined in Appendix A, it is straightforward to show that the contributions to the element load vectors for equations (13) and (14) are

$$F_1^a = -\mu_0\Delta\sigma\Delta z\left[\frac{2\hat{E}_{x1}^p}{\beta_1 + \beta_1^p} + \frac{\hat{E}_{x2}^p}{6\beta_1 + \beta_2^p}\right],$$

$$F_2^a = -\mu_0\Delta\sigma\Delta z\left[\frac{\hat{E}_{x1}^p}{\beta_2 + \beta_2^p} + \frac{2\hat{E}_{x2}^p}{6\beta_2 + \beta_1^p}\right], \qquad \text{(C-8)}$$

$$F_1^b = \frac{ik_x\mu_0|\Delta z|}{\gamma^2}\left[\beta_1\left(\frac{\hat{E}_{y1}^p}{3(\beta_1 + \beta_1^p)} + \frac{\hat{E}_{y2}^p}{6(\beta_2 + \beta_1^p)}\right)\right.$$

$$\left. + \frac{1}{z_1 - z_2}\left(\frac{\hat{E}_{z1}^p}{2(\beta_1 + \beta_1^p)} + \frac{\hat{E}_{z1}^p}{2(\beta_2 + \beta_1^p)}\right)\right], \qquad \text{(C-9)}$$

$$F_2^b = \frac{ik_x\mu_0|\Delta z|}{\gamma^2}\left[\beta_2\left(\frac{\hat{E}_{y1}^p}{6(\beta_1 + \beta_2^p)} + \frac{\hat{E}_{y2}^p}{3(\beta_2 + \beta_2^p)}\right)\right.$$

$$\left. + \frac{1}{z_1 - z_2}\left(\frac{\hat{E}_{z1}^p}{2(\beta_2 + \beta_2^p)} + \frac{\hat{E}_{z1}^p}{2(\beta_2 + \beta_2^p)}\right)\right], \qquad \text{(C-10)}$$

$$F_1^c = \frac{ik_x\Delta z}{2|\Delta y|\gamma^2}\hat{B}_{x2}^s \text{ and } F_2^c = -\frac{ik_x\Delta z}{2|\Delta y|\gamma^2}\hat{B}_{x1}^s, \qquad \text{(C-11)}$$

$$F_1^d = \frac{i\omega|\Delta y|\mu_0\Delta\sigma}{\gamma^2}\left[\frac{\hat{E}_{y1}^p}{2|\Delta z|(\beta_1^p + \beta_1)} + \frac{\hat{E}_{y2}^p}{2|\Delta z|(\beta_2^p + \beta_1)}\right.$$

$$\left. + \frac{\beta_1\hat{E}_{z1}^p}{3(\beta_1^p + \beta_1)} + \frac{\beta_1\hat{E}_{z2}^p}{6(\beta_2^p + \beta_1)}\right], \qquad \text{(C-12)}$$

$$F_2^d = \frac{i\omega|\Delta z|\mu_0\Delta\sigma}{\gamma^2}\left[-\frac{\hat{E}_{y1}^p}{2|\Delta z|(\beta_1^p + \beta_2)} + -\frac{\hat{E}_{y2}^p}{2|\Delta z|(\beta_2^p + \beta_2)}\right.$$

$$+ \frac{\beta_1 \hat{E}_{z1}^p}{3(\beta_1^p + \beta_2)} + \frac{\beta_1 \hat{E}_{z2}^p}{6(\beta_2^p + \beta_2)} \Bigg], \qquad \text{(C-13)}$$

$$F_1^e = \frac{i k, |\Delta z|}{2\Delta z \gamma^2} \hat{E}_{x2}^s \quad \text{a n d} \quad F_2^e = -\frac{i k_x |\Delta z|}{2\Delta z \gamma^2} \hat{E}_{x1}^s. \qquad \text{(C-14)}$$

For a corner element, the element load vector has a single element $F_c = F_c^a + F_c^b + F_c^c + F_c^d + F_c^e$ where,

$$F_c^a = \frac{\mu_0 \Delta \sigma \hat{E}_{xc}^p}{(\beta_y + \beta_y^p)(\beta_z + \beta_z^p)},$$

$$F_c^b = \frac{i k_x \mu \Delta \sigma}{\gamma^2 (\beta_y + \beta_y^p)(\beta_z + \beta_z^p)} [-\beta_y \hat{E}_{yc}^p + \beta_z \hat{E}_{zc}^p] \qquad \text{(C-15)}$$

and

$$F_c^c = 0, \ F_c^d = \frac{i\omega\mu\Delta\sigma}{\gamma^2(\beta_y + \beta_y^p)(\beta_z + \beta_z^p)}$$

$$\times [\beta_z \hat{E}_{yc}^p + \beta_y \hat{E}_{zc}^p] \text{ and } F_c^e = 0 \qquad \text{(C-16)}$$

where $\hat{E}_{xc}^p, \hat{E}_{yc}^p$ and $\hat{E}_{zc}^p$ are the values of the primary electric field at the corner node.